Theoretical study of photoelectron angular distributions in single-photon ionization of aligned N_2 and CO_2

Cheng Jin,[1,2] Anh-Thu Le,[1] Song-Feng Zhao,[1,2] R. R. Lucchese,[3] and C. D. Lin[1]

[1]*J.R. Macdonald Laboratory, Physics Department, Kansas State University, Manhattan, Kansas 66506-2604, USA*

[2]*College of Physics and Electronic Engineering, Northwest Normal University, Lanzhou, Gansu 730070, People's Republic of China*

[3]*Department of Chemistry, Texas A&M University, College Station, Texas 77843-3255, USA*

(Received 19 February 2010; published 25 March 2010)

We calculate photoelectron angular distributions (PADs) resulting from single-photon (43 eV) ionization of molecules that have been transiently aligned with a short laser pulse. The total ionization cross sections of N_2 and CO_2 vs the time delay between the aligning laser pulse and the soft x-ray photon are calculated and compared to experimental results reported by I. Thomann *et al.* [J. Phys. Chem. A **112**, 9382 (2008)]. We present the PADs from these aligned molecules in the laboratory frame which can be compared directly with future experiments from aligned N_2 and CO_2. The alignment dependence of single-photon ionization, multiphoton ionization, and high-order harmonic generation are also analyzed.

DOI: 10.1103/PhysRevA.81.033421 PACS number(s): 33.80.Eh, 42.65.Ky, 33.80.Rv

I. INTRODUCTION

Photoionization (PI) is the basic physical process that allows the most direct investigation of molecular structure [1–4]. Until recently, however, almost all experimental measurements have been performed from an ensemble of randomly distributed molecules. Thus the rich dynamical structure of photoelectron angular distributions (PADs) for fixed-in-space molecules predicted nearly 30 yr ago still remains largely unexplored [5]. Molecular frame photoelectron angular distribution (MFPAD) has been investigated with x-ray or extreme ultraviolet (XUV) photons if the molecular cations dissociate immediately after the absorption of the photon. By using photoion-photoelectron coincidence techniques, the molecular axis can be inferred from the direction of motion of the fragmentation products. Clearly this method is not applicable if the cations are stable, and thus it is not applicable to PI from the highest occupied molecular orbital (HOMO). In the last decade, it has been shown that gas-phase molecules can be aligned with infrared (IR) lasers using either adiabatic or nonadiabatic methods [6–8]. To investigate PI of molecules, the nonadiabatic method is preferable such that PI occurs in field-free conditions.

In a recent experiment, Thomann *et al.* [9] reported the angular dependence of single-photon ionization of aligned N_2 and CO_2 molecules. The molecules were first impulsively aligned by a nonionizing IR laser pulse impinging on supersonically cooled molecules. These aligned molecules were then ionized by 10-fs soft x-ray pulses, and the photoelectrons were detected in coincidence with the molecular ions. The aligning pulse generated a rotational wave packet, which periodically exhibited macroscopic field-free alignment about the polarization axis of the pump laser. The soft x-ray was from high-order harmonic generation (HHG). Filters were used to select only the 27th harmonic (H27) which has a center energy of 43 eV. The ions and electrons were measured during the first half-revival where the molecular-axis distribution changes from aligned to antialigned. In other words, PI can be investigated from partially aligned molecules to probe molecular frame PI directly. Due to the limited number of soft x-ray photons, this measurement did not report PADs from aligned molecules. Similarly, the energy resolution did not permit different ionic states to be distinguished. In spite of this, the experiment did succeed in establishing clearly that PI yield is maximum when the molecules are aligned perpendicular to the polarization of soft x-ray for both N_2 and CO_2 molecules. This is in strong contrast to strong-field multiphoton ionization, where the two molecules show great differences.

In this paper, our first goal is to explain the experimental results of Thomann *et al.* [9] using the well-established PI theory of molecules [10,11]. These theories have been widely used to interpret experimental results for randomly distributed molecules. However, the PI theory also predicts much detail that can be measured from aligned molecules, in particular, the angular distributions of photoelectrons from different subshells. Since the technology of HHG is advancing rapidly, we anticipate that PADs from aligned molecules will become available soon. In this paper, we report the predicted PADs for a pump-probe setup similar to Thomann *et al.* [9]. The predicted angular distributions in the laboratory frame are presented in such a way that they can be compared directly with those obtained in future experiments. In fact, several such measurements have been reported recently [12,13]. Here, we focus on N_2 and CO_2 targets. This would allow us to compare the alignment dependence of single-photon PI by soft x-ray with multiphoton ionization by IR lasers [14,15]. We also examine the alignment dependence of H27 if it is generated by exposing N_2 molecules to intense IR lasers [16]. Since HHG involves a recombination step which is the inverse process of photoionization, such a comparison is of interest.

II. THEORETICAL METHOD

A. Doubly differential photoionization cross section in the molecular frame

The photoionization cross section (PICS) from an initial bound state Ψ_i to the continuum state $\Psi_{f,\vec{k}}^{(-)}$ due to linearly polarized light in the dipole length approximation is proportional

to the square of the dipole matrix elements [10,11]

$$I_{\vec{k},\hat{n}} = (k)^{1/2}\langle\Psi_i|\vec{r}\cdot\hat{n}|\Psi^{(-)}_{f,\vec{k}}\rangle, \tag{1}$$

where $\hat{n}$ is the polarization direction of the light, and $\vec{k}$ is the momentum of the photoelectron. The doubly differential PICS in the molecular (or body-fixed) frame can be expressed as

$$\frac{d^2\sigma}{d\Omega_{\hat{k}}d\Omega_{\hat{n}}} = \frac{4\pi^2 E}{c}|I_{\vec{k},\hat{n}}|^2, \tag{2}$$

where E is photon energy.

To treat the angular dependence of the PICS on the target orientation, the dipole matrix elements are expanded in terms of spherical harmonics

$$I_{\vec{k},\hat{n}} = \left(\frac{4\pi}{3}\right)^{1/2}\sum_{lm\mu} I_{lm\mu}Y^*_{lm}(\Omega_{\hat{k}})Y^*_{l\mu}(\Omega_{\hat{n}}). \tag{3}$$

The partial-wave matrix elements are given by

$$I_{lm\mu} = (k)^{1/2}\langle\Psi_i|r_\mu|\Psi^{(-)}_{f,klm}\rangle, \tag{4}$$

where

$$r_\mu = \begin{cases} \mp(x \pm iy)/2^{1/2} & \mu = \pm 1, \\ z & \mu = 0. \end{cases} \tag{5}$$

In the calculation, the initial bound state Ψ_i is obtained from the MOLPRO code [17] within the valence complete-active-space self-consistent field (CASSCF) method. Based on the frozen-core approximation, the final state $\Psi^{(-)}_{f,\vec{k}}$ is then described in a single-channel approximation where the wave function of the ionic core is given by a valence complete active space configuration interaction (CI) wave function obtained using the same bound orbitals as in the initial state. It has the form

$$\Psi^{(-)}_{f,\vec{k}} = \mathbf{A}[\Phi\phi^{(-)}_{\vec{k}}(\vec{r})], \tag{6}$$

where Φ is the correlated $N-1$ electron ionic-core wave function, $\phi^{(-)}_{\vec{k}}(\vec{r})$ is the one-electron continuum wave function, and operator $\mathbf{A}$ performs the appropriate antisymmetrization of spin and spatial symmetry adaptation of the product of the ionic-core and continuum wave functions. Note that it is possible to use ionic orbitals; however, we perform CI calculations in both the initial and final states; the choice of orbitals does not affect much the final results. For valence ionization, such as we are studying here, the position of one-electron continuum resonances has been reproduced quite well using the initial-state orbitals. So starting with initial-state orbitals and using CI wave functions give quite reliable results.

The Schrödinger equation for the remaining continuum electron is then (in atomic units)

$$\left[-\frac{1}{2}\nabla^2 - \frac{1}{r} + V(\vec{r}) - \frac{k^2}{2}\right]\phi^{(-)}_{\vec{k}}(\vec{r}) = 0, \tag{7}$$

where $V(\vec{r})$ is the short-range portion of the electron-molecular-ion interaction. Note that the potential is not spherically symmetric for molecules. Equation (7) is then solved by using the iterative Schwinger variational method. The continuum wave function is expanded in terms of partial waves as

$$\phi^{(-)}_{\vec{k}}(\vec{r}) = \left(\frac{2}{\pi}\right)^{1/2}\sum_{l=0}^{l_p}\sum_{m=-l}^{l} i^l\phi^{(-)}_{klm}(\vec{r})Y^*_{lm}(\Omega_{\hat{k}}), \tag{8}$$

where an infinite sum over l has been truncated at $l = l_p$. In the calculation, we typically choose $l_p = 11$. Once we obtain $\phi^{(-)}_{klm}(\vec{r})$, then $\Psi^{(-)}_{f,klm}$ in Eq. (4) can be obtained straightforwardly through Eq. (6). Note that our continuum wave function is constructed to be orthogonal to the strongly occupied orbitals. This avoids spurious singularities which can occur when scattering from correlated targets is considered [18].

Here we describe the method used to compute the scattering potential $V(\vec{r})$ found in Eq. (7). First, the electronic Hamiltonian is written as

$$H = \sum_{i=1}^{N} h(i) + \sum_{i<j}^{N}\frac{1}{r_{ij}}, \tag{9}$$

with

$$h(i) = -\frac{\nabla_i^2}{2} - \sum_a \frac{Z_a}{r_{ia}}, \tag{10}$$

where the Z_a are the nuclear charges, and N is the number of electrons. Then the single-particle equation for the continuum electron is obtained from

$$\langle\delta\Psi^{(-)}_{f,\vec{k}}|H - E|\Psi^{(-)}_{f,\vec{k}}\rangle = 0, \tag{11}$$

where $\delta\Psi^{(-)}_{f,\vec{k}}$ is written as in Eq. (6), with $\phi^{(-)}_{\vec{k}}(\vec{r})$ replaced by $\delta\phi^{(-)}_{\vec{k}}(\vec{r})$. By requiring this equation to be satisfied for all possible $\delta\Psi^{(-)}_{f,\vec{k}}$ [or $\delta\phi^{(-)}_{\vec{k}}(\vec{r})$], one obtains a nonlocal optical potential that can be written in the form of a Phillips-Kleinman pseudopotential [19,20].

A single-center expansion approach is used to evaluate all required matrix elements. In other words, all functions, including the scattering wave function, occupied orbital, and potential are expanded about a common origin, which is the center of mass of the molecule, as a sum of spherical harmonics times radial functions

$$F(\vec{r}) = \sum_{l=0}^{l_{\max}}\sum_{m=-l}^{l} f_{lm}(r)Y_{lm}(\theta,\phi). \tag{12}$$

With this expansion, the angular integration can be done analytically, and all three-dimensional integrals reduce to a sum of radial integrals, which are computed on a radial grid. Typically, we choose $l_{\max} = 60$–85.

If we are dealing with electron ionization from inner molecular orbitals, i.e., not HOMO, but rather HOMO-1 and HOMO-2, it can still be done in the same manner, except that the ionic-core state Φ employed in Eq. (6) needs to be replaced by the excited-ion state, which corresponds to electron ionization from the HOMO-1 or HOMO-2 orbital. Furthermore, the present single-channel formalism can be extended to coupled-multichannel calculations to account for additional electron correlation effects [21]. The calculations in this paper are limited to the single-channel approximation.

TABLE I. Molecular properties for N_2 and CO_2. B is the rotational constant, $\alpha_\parallel$ and $\alpha_\perp$ are parallel and perpendicular polarizability, respectively. The data are from [26,27].

Molecule	B (cm^{-1})	$\alpha_\parallel$ (Å^3)	$\alpha_\perp$ (Å^3)
N_2	1.989	2.38	1.45
CO_2	0.39	4.05	1.95

B. Angular distribution of linear molecules in a laser field

When linear molecules are placed in a short laser field (pump laser), a rotational wave packet is excited. At later times when the wave packet undergoes "rotational revival" [22,23], the molecules will be aligned or antialigned. To calculate the alignment, or the angular distribution of the molecules, each molecule can be treated as a rigid rotor [24,25]. The time-dependent Schrödinger equation describing the evolution of a rotational wave packet with initial state $\Psi_{JM}(\theta, \varphi, t = -\infty)$ in a linearly polarized laser field is given by

$$i\frac{\partial \Psi_{JM}(\theta,\varphi,t)}{\partial t} = \left[B\mathbf{J}^2 - \frac{E(t)^2}{2}(\alpha_\parallel \cos^2\theta + \alpha_\perp \sin^2\theta)\right] \times \Psi_{JM}(\theta,\varphi,t), \quad (13)$$

where $\mathbf{J}$ is the angular momentum operator, B is the rotational constant, and $\alpha_\parallel$ and $\alpha_\perp$ are the anisotropic polarizabilities in parallel and perpendicular directions with respect to the molecular axis, respectively. These molecular properties for N_2 and CO_2 are shown in Table I. $E(t)$ in Eq. (13), the electric field of the pump laser, is taken to have a Gaussian form:

$$E(t) = E_0 e^{-(2\ln 2)t^2/\tau_w^2}\cos(\omega_0 t), \quad (14)$$

where E_0 is the peak field, τ_w and ω_0 are the pulse duration (full width at half maximum, FWHM) and frequency of the pump laser, respectively. Equation (13) is written in the molecular (or body-fixed) frame.

Equation (13) is solved independently for each initial rotational state $|JM\rangle$ (up to $J = 40$) using the split-operator method [28,29]. After the pump laser is turned off, the rotational wave packet will continue to propagate in the free space,

$$\Psi_{JM}(t) = \sum_{J'} a_{J'} e^{-iE_{J'}t}|J'M\rangle, \quad (15)$$

where $E_{J'}$ are the energy eigenvalues, $|J'M\rangle$ are spherical harmonics, and the coefficients of $a_{J'}$ can be determined at the moment when the pump laser is turned off.

Assuming a Boltzmann distribution of the rotational levels at the initial time, the time-dependent alignment at a given temperature can be obtained by

$$\rho(\theta, t) = \sum_{JM} \omega_{JM}|\Psi_{JM}(\theta,\varphi,t)|^2, \quad (16)$$

where ω_{JM} is the weight according to the Boltzmann distribution. The nuclear statistics and symmetry of the total electronic wave function must be taken into account properly in order to determine ω_{JM}. The angular distribution or alignment does not depend on the azimuthal angle φ in the frame attached to the pump laser field, and it only depends on the angle θ between the molecular axis and the polarization direction of the pump laser.

C. Alignment dependence of integrated photoionization cross section

The doubly differential PICS in the molecular frame is given in Eq. (2), but for a given application, one may need averaged PICSs as suggested by Wallace and Dill [30]. One such averaged distribution is the integrated detector angular distribution (IDAD), which corresponds to experiments where target orientation is fixed in space and the PICS is integrated over all possible emission directions of photoelectron. For linear molecules, the integrated cross section depends only on the alignment angle θ due to the symmetry of the molecules, and the IDAD can be expressed in the molecular frame as

$$\sigma(\theta, E) = \frac{d\sigma}{d\Omega_{\hat{n}}} = \int \frac{4\pi^2 E}{c}|I_{\vec{k},\hat{n}}|^2 d\Omega_{\hat{k}}. \quad (17)$$

Equation (17) can also be found in the form of [10,30]

$$\frac{d\sigma}{d\Omega_{\hat{n}}} = \frac{\sigma_{\rm tot}}{4\pi}[1 + \beta_{\hat{n}} P_2(\cos\theta)], \quad (18)$$

where $\sigma_{\rm tot}$ is the total PICSs averaged over all alignments and photoelectron directions, $P_2(\cos\theta)$ is the Legendre polynomial of degree 2, and $\beta_{\hat{n}}$ is the asymmetry parameter.

In experiments, the pump laser is used to create a transiently aligned molecular sample, and then the soft x-ray probe ionizes the molecules. The time-dependent alignment distribution is obtained by Eq. (16). If the polarizations of the pump and probe lasers are parallel, the detected experimental signal in terms of the pump-probe time delay τ can be written as

$$Y(E, \tau) \propto \int_0^\pi \sigma(\theta, E)\rho(\theta, \tau)\sin\theta\, d\theta. \quad (19)$$

Without the pump-probe scheme, the molecules are distributed randomly, and the angular distribution of $\rho(\theta, \tau)$ in Eq. (19) is a constant. Equation (19) actually gives us the total cross section $\sigma_{\rm tot}$.

D. Photoelectron angular distribution in the laboratory frame

The PICS in the molecular frame is given in Eq. (2), and the doubly differential PICS in the laboratory frame can be expressed as

$$\frac{d^2\sigma}{d\Omega_{\hat{k}'}d\Omega_{\hat{n}'}} = \frac{4\pi^2 E}{c}|I_{\vec{k}',\hat{n}'}|^2, \quad (20)$$

where $\hat{n}'$ and $\vec{k}'$ are the polarization direction of pump laser and the momentum of the photoelectron in the laboratory frame, respectively. We assume that the molecular axis is aligned at an arbitrary angle $\hat{\mathbf{R}} \equiv (\theta, \varphi)$ with respect to the polarization direction of the pump laser. In other words, $\hat{\mathbf{R}}$ is the Euler angle of the molecular frame with respect to the laboratory frame. The dipole matrix elements in Eq. (3) can be rewritten in the

laboratory frame as

$$I_{\vec{k}',\hat{n}'} = \left(\frac{4\pi}{3}\right)^{1/2} \sum_{lm\mu} I_{lm\mu} \sum_{m'=-l}^{l} D^{l}_{mm'}(\hat{\mathbf{R}}) Y^{*}_{lm'}(\theta_{k'}, \varphi_{k'}) \times \sum_{\mu'=-l}^{l} D^{l}_{\mu\mu'}(\hat{\mathbf{R}}) Y^{*}_{l\mu'}(\theta_{n'}, \varphi_{n'}), \quad (21)$$

with $D^{l}_{mm'}(\hat{\mathbf{R}})$ and $D^{l}_{\mu\mu'}(\hat{\mathbf{R}})$ being the rotation matrices. In Eq. (21), $\theta_{k'}$ and $\varphi_{k'}$ are the polar and azimuthal angles of the photoelectron in the laboratory frame, respectively, $\theta_{n'} = 0^{\circ}$ and $\varphi_{n'} = 0^{\circ}$ in the laboratory frame. The PICS of Eq. (20) in the laboratory frame is an explicit function of $\theta_{k'}$ and $\varphi_{k'}$ for the alignment angle $\hat{\mathbf{R}}$.

In the laboratory frame, taking into account the molecular distribution with respect to the polarization direction of the pump laser described by the angle θ, the PICS in Eq. (20) must be integrated over the azimuthal angle φ. Finally, we obtain the PICS for all molecules with a fixed alignment angle θ, which depends on photoelectron emission angle $\theta_{k'}$,

$$\sigma'(\theta, E, \theta_{k'}) = \int_0^{2\pi} \frac{d^2\sigma}{d\Omega_{\hat{k}'}\, d\Omega_{\hat{n}'}}(\theta, \theta_{k'}, \varphi_{k'} - \varphi)\, d\varphi. \quad (22)$$

The actual experimentally observed photoelectron angular distribution in the laboratory frame (LF-PAD) corresponds to the average of the PICSs in Eq. (22) accounting for the molecular distribution in space. The time-dependent angular distribution of $\rho(\theta, \tau)$ can be calculated by Eq. (16), and the analytical form of the LF-PAD, which can be compared directly with experimental photoelectron spectra, is expressed as

$$Y'(E, \theta_{k'}, \tau) \propto \int_0^{\pi} \sigma'(\theta, E, \theta_{k'}) \rho(\theta, \tau) \sin\theta\, d\theta. \quad (23)$$

The polarizations of the pump and probe lasers are parallel in Eq. (23).

As suggested by Wallace and Dill [30], another averaged PICS is the integrated target angular distribution (ITAD), which corresponds to PI experiments where target orientation is not resolved. For the isotropically distributed molecules, the angular distribution of $\rho(\theta, \tau)$ is a constant, and Eq. (23) has the form [10,30]

$$\frac{d\sigma}{d\Omega_{\hat{k}'}} = \frac{\sigma_{\text{tot}}}{4\pi}[1 + \beta_{\hat{k}'} P_2(\cos\theta_{k'})], \quad (24)$$

where $\beta_{\hat{k}'}$ is the photoelectron asymmetry parameter.

E. Photoionization by XUV photons and harmonic generation in molecules

HHG can be understood based on the rescattering concept [31–33]. Recently we have established a quantitative rescattering (QRS) theory for HHG [34,35] in which the induced dipole moment $D(\omega, \theta)$ of a fixed-in-space molecule in the intense laser field can be expressed as

$$D(\omega, \theta) = W(\omega, \theta)\, d(\omega, \theta), \quad (25)$$

or written out with the phase and amplitude of each term explicitly,

$$|D(\omega, \theta)|e^{i\varphi(\omega,\theta)} = |W(\omega, \theta)|e^{i\eta}|d(\omega, \theta)|e^{i\delta(\omega,\theta)}. \quad (26)$$

Here $|W(\omega, \theta)|^2$ describes the flux of returning electrons with θ being the molecular alignment angle with respect to the laser polarization, and it is proportional to the alignment-dependent tunneling ionization rate N(θ) [36,37], and ω is the frequency of the harmonic. In the equations above, $\varphi(\omega, \theta)$ is the phase of the induced dipole, and $d(\omega, \theta)$ and $\delta(\omega, \theta)$ are the photorecombination transition dipole and its phase, respectively. Since photorecombination in the production of HHG is the time-reversed process of PI, $d(\omega, \theta)$ can be calculated from the established PI theory [10,11]. For the purpose of illustrating the connection between PI and HHG, we focus on the HHG component that is parallel to the laser's polarization only. In the calculation of the HHG, we need a doubly differential PICS in Eq. (2) for $\vec{k} \parallel \hat{n}$ or in Eq. (20) for $\vec{k}' \parallel \hat{n}'$.

HHG from aligned N_2 and CO_2 has been reported experimentally [38–45], and QRS theory has been applied to interpret some of these measurements [16,35]. Thus HHG from aligned molecules also provides a direct test of the accuracy of dipole matrix elements calculated from molecular PI theory. On the other hand, one must be careful since the HHG measured in an experiment is affected by the propagation effect in the macroscopic medium [46].

III. RESULTS AND DISCUSSION

A. Connection between photoionization and harmonic generation

For aligned molecules, experimentally one can measure the ionization cross section by single photons, say, at 43 eV, by multiphotons with IR lasers, say, at 800 nm (1.55 eV per photon), or by the observation of high-order harmonics, say, H27, at 43 eV. Today field-free molecules can be transiently aligned by lasers only, thus experiments are carried out at intense IR laser facilities. To compare with experimental measurements, theory must perform calculations first on molecules that are fixed in space. Here we compare photoionization cross sections (PICSs) for ionization by a 43-eV photon of N_2 leaving N_2^+ in the $X^2\Sigma_g^+$, $A^2\Pi_u$, and $B^2\Sigma_u^+$ ionic states, corresponding to removing an electron from the HOMO, HOMO-1, and HOMO-2 orbitals of N_2, respectively. In Fig. 1(a), we show the alignment dependence of integrated PICSs for ionization leading to the X, A, and B states of the ion. The polarization axis is fixed, and the molecular axis makes an angle θ with respect to it. According to Eq. (18), we obtain the asymmetry parameter $\beta_{\hat{n}}$ to be -0.83, -0.95, and 0.47 for X, A, and B states, respectively [10].

From Fig. 1(a), we note that PICSs are of the same order of magnitude, with the HOMO and HOMO-1 channels having nearly identical θ dependence even though HOMO is a σ_g orbital and HOMO-1 is a π_u orbital. This is in strong contrast with ionization by intense IR lasers. Figure 1(c) shows the alignment-dependent multiphoton ionization rates of N_2 by intense lasers with peak intensity of 2×10^{14} W/cm^2 calculated with molecular tunneling ionization theory [36,37], which is also well known as the molecular Ammosov-Delone-Krainov (MO-ADK) theory. Note that ionization rates for X, A, and B states are quite different since tunneling is the main mechanism for ionization at such high intensities. For

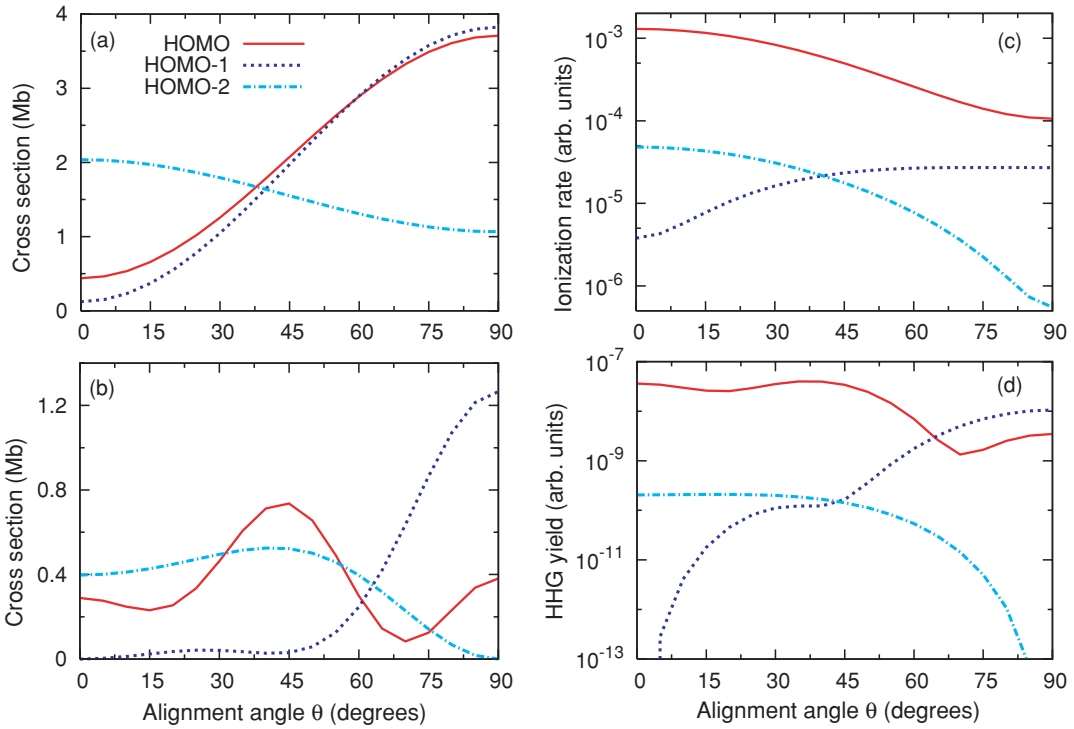

FIG. 1. (Color online) (a) Integrated photoionization cross sections and (b) doubly differential cross sections for electrons ejected in the polarization direction for N_2 aligned at an angle θ from the polarization axis, by a single photon at 43 eV. (c) Alignment dependence of the multiphoton ionization rate of N_2 by a laser with intensity of 2×10^{14} W/cm^2. (d) Alignment dependence of the 27th harmonic (43 eV) of N_2 by a laser with intensity of 2×10^{14} W/cm^2, wavelength of 800 nm, and duration (FWHM) of 30 fs. HOMO (solid lines), HOMO-1 (dotted lines), and HOMO-2 (dot dashed lines).

the tunneling processes, the ionization rate decreases rapidly as the ionization energy increases. The A and B states are higher than the X state (15.6 eV) by 1.3 eV and 3.2 eV, respectively [47]. On the other hand, the alignment dependence of strong field ionization reflects the shape of the charge density of the molecular orbital from which the electron is removed, as stated earlier.

Next we consider the alignment dependence of HHG. According to Eq. (25), the HHG yield is proportional to the product of tunneling ionization rate [see Fig. 1(c)] and the differential PICSs for electrons ejected along the polarization axis [see Fig. 1(b)] (the modulus square of photoionization transition dipole is proportional to differential PICS). The resulting alignment dependence of H27 is shown in Fig. 1(d). It shows that at the intensity of 2×10^{14} W/cm^2, HOMO-1 overtakes HOMO in contributing to the generation of H27 when molecules are aligned near 90°. Using the QRS theory, Le *et al.* [16] were able to explain these results observed experimentally by McFarland *et al.* [38]. We comment that the HHG contributions from the three orbitals shown in Fig. 1(d) should have been added coherently. Coherence can be neglected in regions where there is only one dominant channel.

One advantage of studying HHG is that the phase of the dipole transition matrix element can be retrieved from the phase of the harmonics, see Refs. [35,39,44,48]. On the other hand, unlike photoionization, experimental HHG spectra suffer from the macroscopic propagation effect [46] and thus care must be taken when drawing conclusions on single-molecule HHG spectra from experimental HHG spectra.

B. Total photoionization cross sections from aligned N_2 and CO_2 molecules

Thomann *et al.* [9] employed a state-of-the-art high-harmonic ultrafast soft x-ray to ionize field-free aligned molecules in which the cations are nondissociative. In their experiment, a single harmonic order—H27 at 43 eV—with a width of a few eV, was selected as the ionizing probe pulse. The ion yield was detected around the first half-revival of 4.2 ps for N_2 and 21.0 ps for CO_2. The polarization axes for the aligning and ionizing pulses were parallel such that molecular distributions had cylindrical symmetry with respect to the polarization axis. They presented the yields of singly ionized N_2 and CO_2 by 43-eV photons as a function of time delay between the two pulses. In this section, we report the comparison between our theoretical calculations and their experimental results.

In Fig. 2(a), we show the calculated degree of alignment $\langle \cos^2 \theta \rangle$ for N_2 vs time delay. In the calculation, the pump laser has a wavelength of 800 nm, duration (FWHM) of 140 fs, and intensity of 5×10^{12} W/cm^2, taken from Ref. [9]. We choose a gas temperature of 20 K to obtain a high degree of alignment. By solving Eq. (13), $\langle \cos^2 \theta \rangle$ can be calculated from Eq. (16). In Fig. 2(c), the alignment-dependent PICSs (summed over X, A, and B ionic states) are shown. Combining with the calculated alignment distribution of molecules, we obtain the photoionization yield vs time delay. The results are shown in Fig. 2(b) and compared to experimental data of Ref. [9]. Clearly the theoretical calculations are in good agreement with experiment. It shows that when molecules

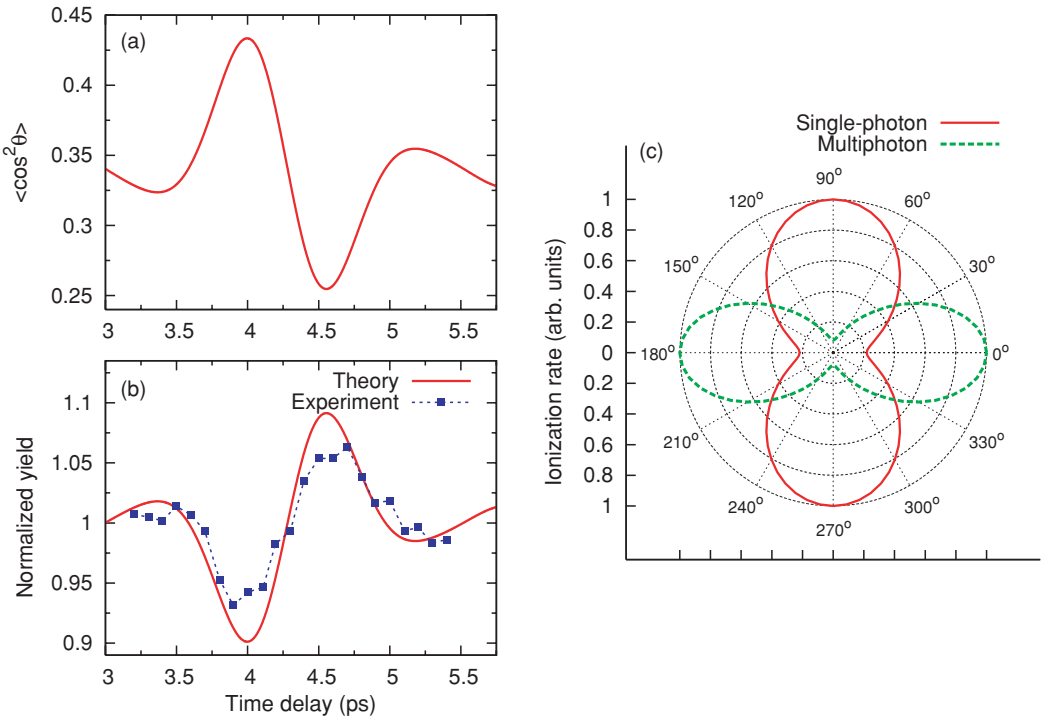

FIG. 2. (Color online) (a) Calculated degree of alignment $\langle\cos^2\theta\rangle$ for N_2 vs time delay near first half-revival. (b) Single-photon ionization yield from transiently aligned N_2 by 43-eV photons vs time delay: theory (solid line) and experiment (solid squares) [9]. (c) Angular dependence of the ionization rate in single-photon (43-eV) ionization (solid line), and by multiphoton ionization by an IR laser with intensity of 2×10^{14} W/cm^2 (dashed line).

are aligned mostly perpendicular to the polarization axis, the total ionization yield peaks. This is easily understood from Fig. 1(a), or from Fig. 2(c), which shows the sum of ionization cross sections (normalized at $\theta = 90^\circ$) from the X, A, and B ionic states. For comparison, the alignment dependence of multiphoton ionization rates (normalized at $\theta = 0^\circ$) by intense IR lasers at peak intensity of 2×10^{14} W/cm^2 are also shown in Fig. 2(c). In this case, ionization occurs mostly from the X ionic state, i.e., only from the HOMO orbital.

Similar calculations have been carried out for CO_2 molecules. The parameters for the pump laser are wavelength of 800 nm, duration (FWHM) of 140 fs, and intensity of 3.5×10^{12} W/cm^2. The gas temperature is chosen to be 20 K. PICSs at each fixed alignment angle θ for ionization leading to CO_2^+ in the $X\ ^2\Pi_g$, $A\ ^2\Pi_u$, and $B\ ^2\Sigma_u^+$ ionic states are shown in Fig. 3(c). The asymmetry parameters $\beta_{\hat{n}}$ extracted from Fig. 3(c) are -0.64, -0.77, and -0.53 for the X, A, and B states, respectively. And the θ dependence of the ionization cross sections (summed over X, A, and B states, and normalized at $\theta = 90^\circ$) are shown in polar plot in Fig. 3(d). In Fig. 3(d), the total multiphoton ionization rate (normalized at $\theta = 35^\circ$) vs θ for an IR laser with intensity of 1.1×10^{14} W/cm^2 is also shown. The latter has the shape of a butterfly, reflecting the angular dependence of the π_g orbital of the HOMO. Note that in adding up cross sections from different channels, the degeneracy of the molecular orbitals should be included.

The $\langle\cos^2\theta\rangle$ and the total ionization yield vs time delay for CO_2 are shown in Figs. 3(a) and 3(b), respectively. Both have behavior that is quite similar to the behavior seen in Figs. 2(a) and 2(b) for N_2. The calculated results in Fig. 3(b) are in good agreement with the results from Ref. [9]. Note that the alignment dependence of multiphoton ionization for individual X, A, and B ionic states are actually quite different, and they have different orbital symmetries. To obtain the tunneling ionization rate from the MO-ADK theory shown in Fig. 3(d), the vertical ionization energies are taken from [11,47], while the molecular parameters are from Zhao *et al.* [37].

C. Photoelectron angular distributions (PADs) of fixed-in-space N_2 molecules in the laboratory frame

Experimentally, cold target recoil ion momentum spectroscopy (COLTRIMS) has been used to measure the full momentum vectors of charged particles resulting from the ionization of molecules [49]. For different ionization channels, the detected photoelectron energy $E_{\rm pe}$ is related to photon energy $h\nu$ and vertical ionization energy $E_{\rm ion}$ by $E_{\rm pe} = h\nu - E_{\rm ion}$. The PADs from different ionization channels can be measured. We present the results in the laboratory frame so they can be compared with future measurements.

In Fig. 4, we show the PADs from fixed-in-space N_2 molecules that make an angle θ with the polarization axis. Photons of 43 eV are used and the ions are left in the X, A, and B ionic states after PI. Figures 4(a)–4(c) compare the PADs for emission angles from 0° to 90° for several molecular alignments. As the alignment angle changes, the PAD changes rapidly. The PADs for the three channels at a given molecular alignment angle also vary significantly. For easier comparison of the complicated PAD, false colors are used to present the PAD for each ionic state, see Figs. 4(d)–4(g). The radius

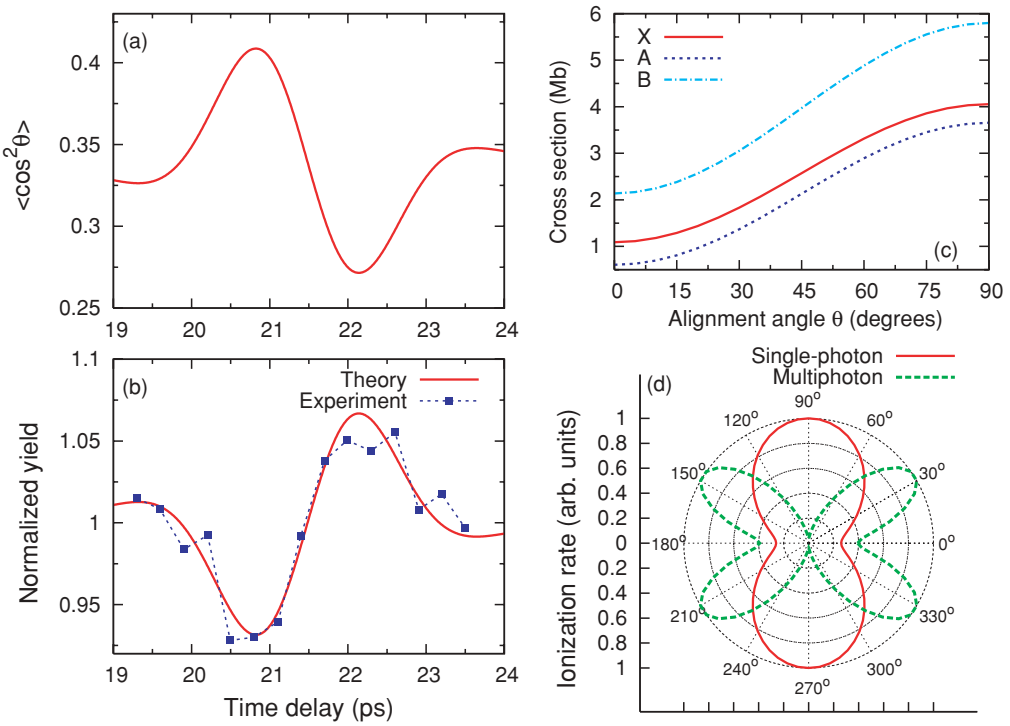

FIG. 3. (Color online) (a) Calculated degree of alignment $\langle \cos^2 \theta \rangle$ for CO_2 vs time delay near first half-revival. (b) Single-photon ionization yield from transiently aligned CO_2 by 43-eV photons vs time delay: theory (solid line) and experiment (solid squares) [9]. (c) Integrated photoionization cross section for ionization leading to the X (solid line), A (dotted line), and B (dot-dashed line) ionic states of CO_2^+, with alignment angle θ, by single-photon (43-eV) ionization of CO_2. (d) Angular dependence of the ionization rate for single-photon (43-eV) ionization (solid line), and for multiphoton ionization by an IR laser with intensity of 1.1×10^{14} W/cm^2 (dashed line).

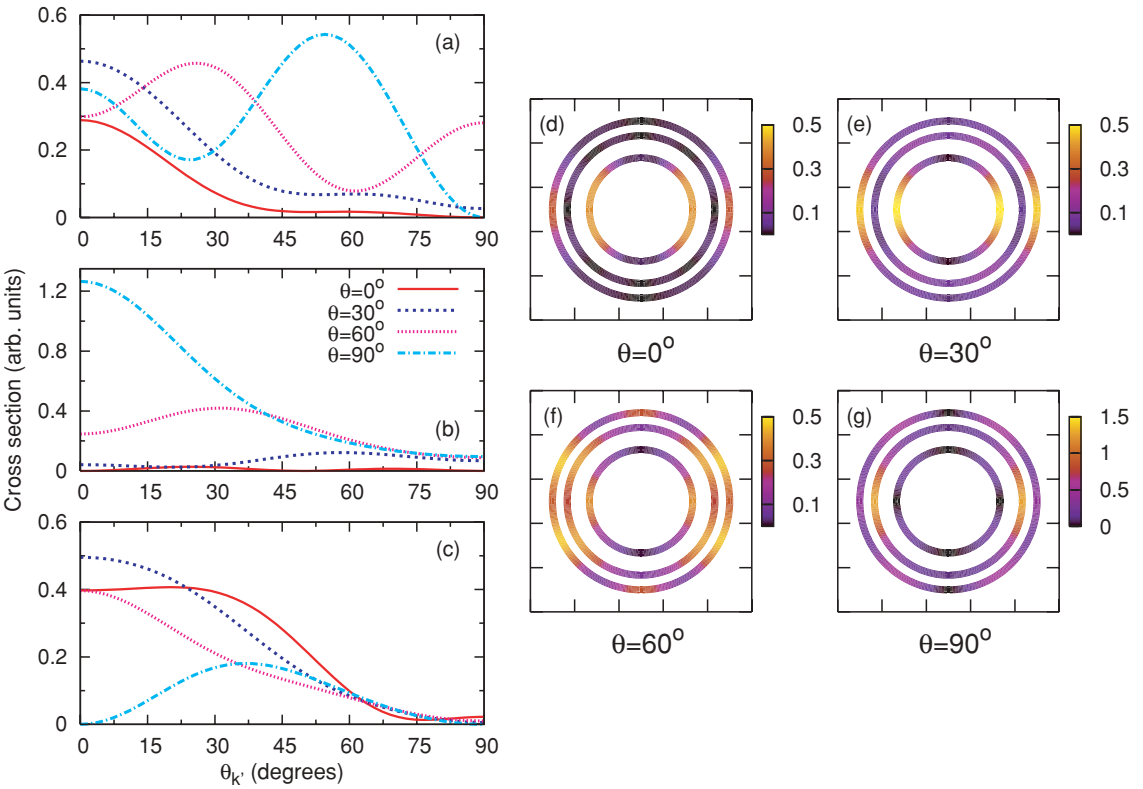

FIG. 4. (Color online) Photoionization cross sections in the laboratory frame for single-photon (43-eV) ionization of fixed-in-space N_2 vs emission angle $\theta_{k'}$ at alignment angles indicated and for ionization leading to N_2^+ in the X, A, and B states, shown in panels (a)–(c), respectively. In panels (d)–(g) the same distributions are shown for the X, A, and B channels at each fixed-in-space molecular alignment angle. See text.

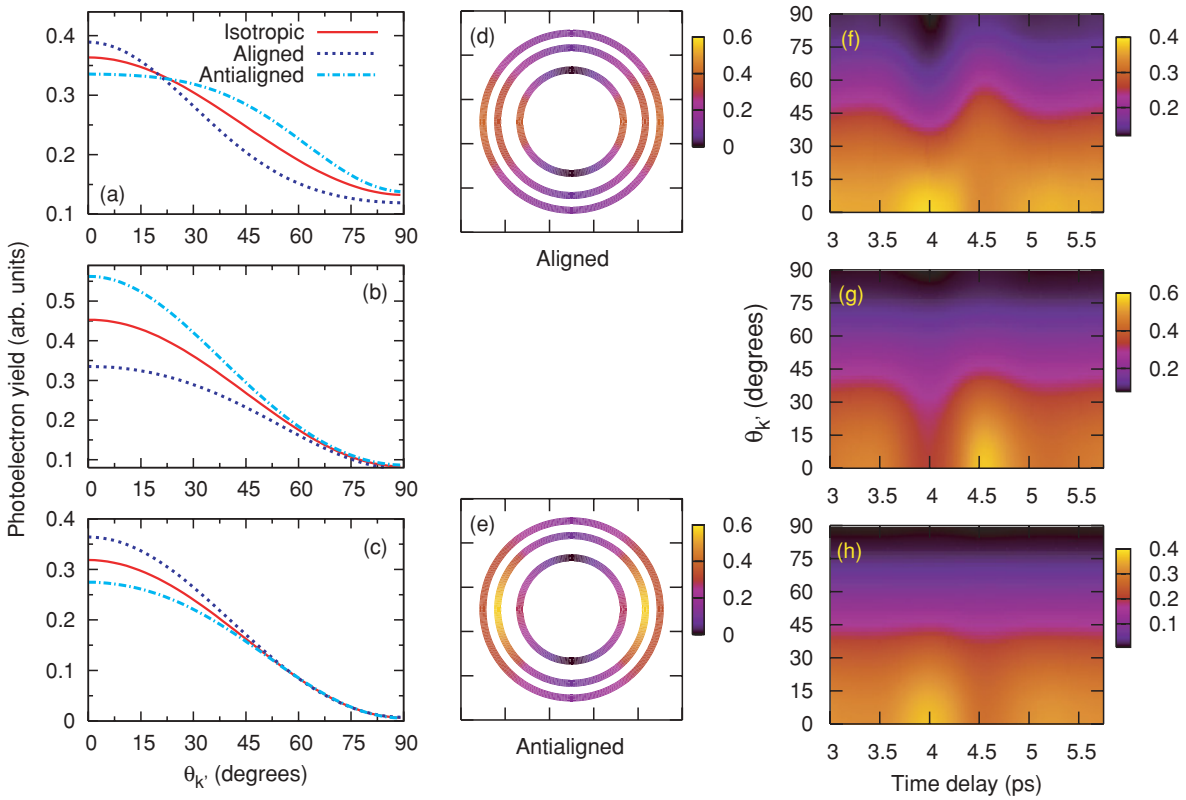

FIG. 5. (Color online) PADs in the laboratory frame for single-photon (43-eV) ionization of N_2 as a function of emission angle $\theta_{k'}$ and pump-probe time delay. (a)–(c): Molecules are maximally aligned ($\tau = 4.00$ ps), antialigned ($\tau = 4.55$ ps), and isotropically distributed, for ionization leading to N_2^+ ions in X, A, and B states, respectively. (d) and (e): The same distributions are compared for maximally aligned and antialigned molecules. (f)–(h): PADs vs time delay for the X, A, and B channels, respectively.

measures the photoelectron energies. Thus the rings, starting from the outermost, are for electrons ejected from HOMO, HOMO-1, and HOMO-2, respectively. These complicated variations of the PADs from aligned molecules is in strong contrast with PI from isotropically distributed molecules where the PAD depends on a single β parameter and can be expressed as in Eq. (24).

D. PADs of transiently aligned N_2 molecules in the laboratory frame

For transiently aligned molecules, the angular distribution of molecules with respect to the laser polarization axis evolves with time delay. To compare with experimental measurements, the PAD for each fixed angle must be averaged over the molecular alignment distributions. In Figs. 5(a)–5(c), we show the PADs after such averaging for the X, A, and B ionic states, respectively, at the two time delays when molecules are maximally aligned or antialigned. Note that the angular averaging has severely smoothed out the structures compared to the "raw" data shown in Fig. 4. In Figs. 5(a)–5(c) we also show the PADs for molecules that are isotropically distributed for comparison. Using Eq. (24), we found the values of $\beta_{k'}$ to be 0.74, 1.20, and 1.88 for the X, A, and B channels, respectively [10]. In Figs. 5(d) and 5(e), the PADs from the three ionic states are compared together. Such data can be compared directly with future experiments, since the PADs have been expressed in the laboratory frame with the fixed polarization axis. Alternatively, the laboratory-fixed PAD for each ionic state vs the time delay can also be measured, and they are shown in Figs. 5(f)–5(h). While the degree of molecular alignment by IR lasers is not very sharp, in the future, data like those in Figs. 5(f)–5(h) can be deconvoluted to retrieve PADs for fixed molecular alignment angles, and to compare with theoretical calculations shown in Figs. 4(a)–4(c).

In Fig. 5, we assume that the pump laser to align the molecules is the same as that assumed in Fig. 3. The maximum degree of alignment is only $\langle \cos^2\theta \rangle = 0.43$, such that no striking features are seen. To improve the contrast, we assume a pump laser with intensity of 5×10^{13} W/cm^2, duration of 60 fs at temperature of 20 K to align molecules. The maximum degree of alignment achieved is $\langle \cos^2\theta \rangle = 0.71$. We show the PADs in the laboratory frame in Fig. 6. Molecules are maximally aligned at $\tau = 4.04$ ps and antialigned at $\tau = 4.39$ ps. In comparison with Fig. 5, with the better alignment, we can clearly see the improved contrast, and PADs of aligned and antialigned molecules become closer to those for fixed-in-space molecules at $\theta = 0^\circ$ and 90°, respectively, see Fig. 4.

E. Photon energy dependence of PADs for aligned N_2 molecules

All the calculations above have been carried out at a photon energy of 43 eV. Next we explore the behavior of the alignment dependence of the PAD at photon energies of 20, 30, and 46 eV. In Fig. 7, the PADs for the X, A, and B channels are shown for

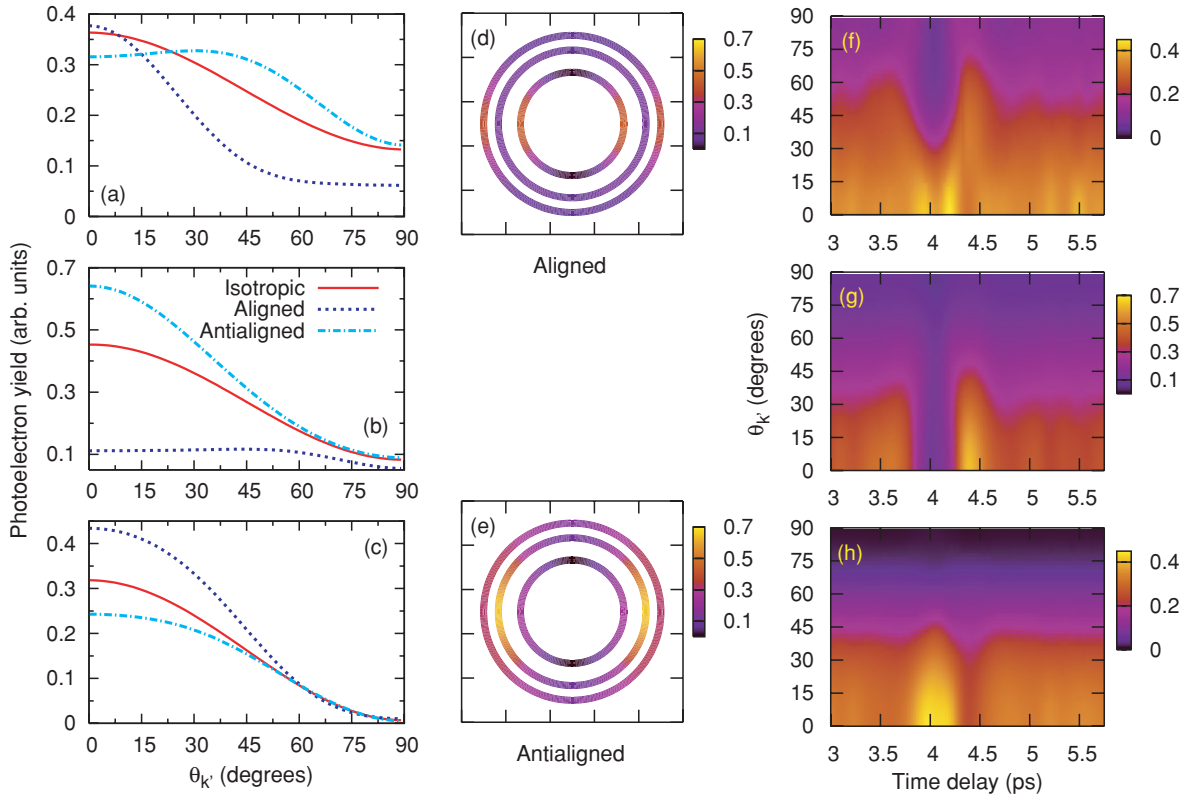

FIG. 6. (Color online) Same as Fig. 5 except that a strong aligning pump laser is assumed. See text.

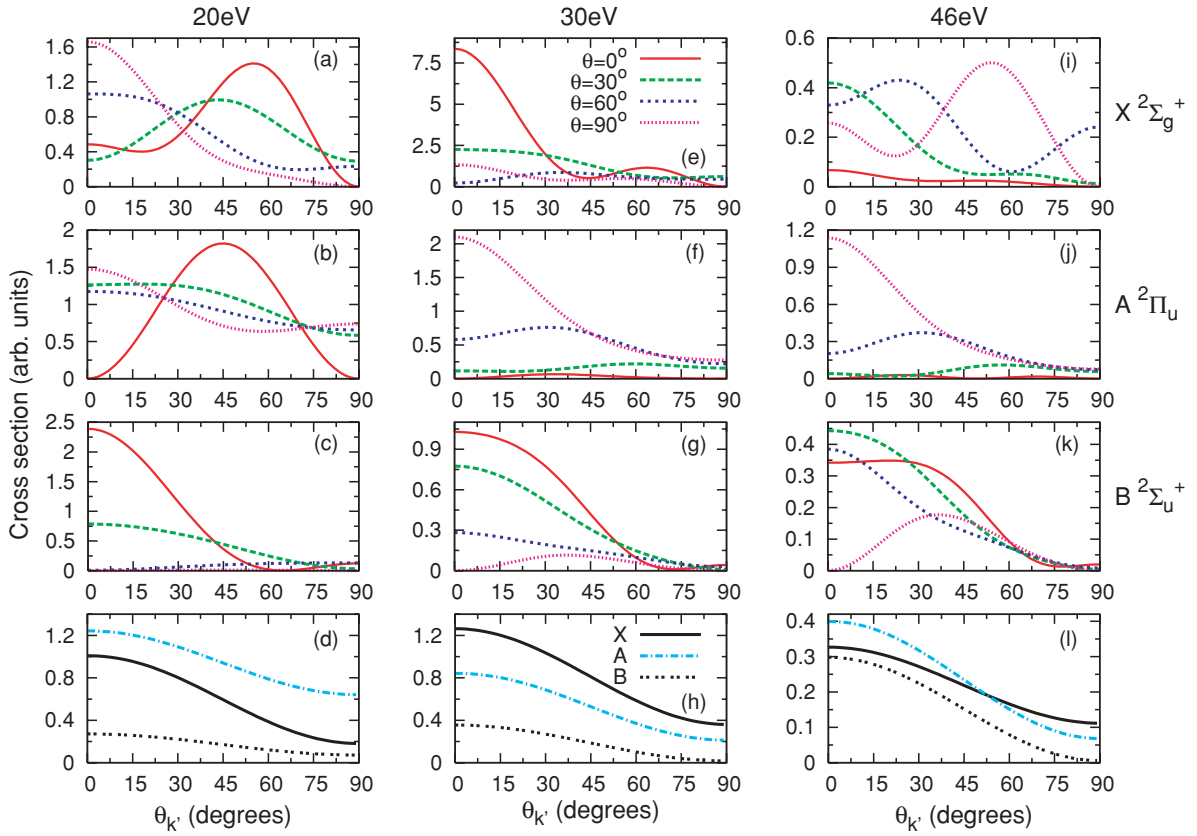

FIG. 7. (Color online) Fixed-in-space photoionization angular distributions (vs $\theta_{k'}$) in the laboratory frame, for photon energies of 20, 30, or 46 eV, and the four alignment angles shown. First row: *X* channel. Second row: *A* channel. Third row: *B* channel. The last row shows that the PAD becomes featureless if the molecules are isotropically distributed.

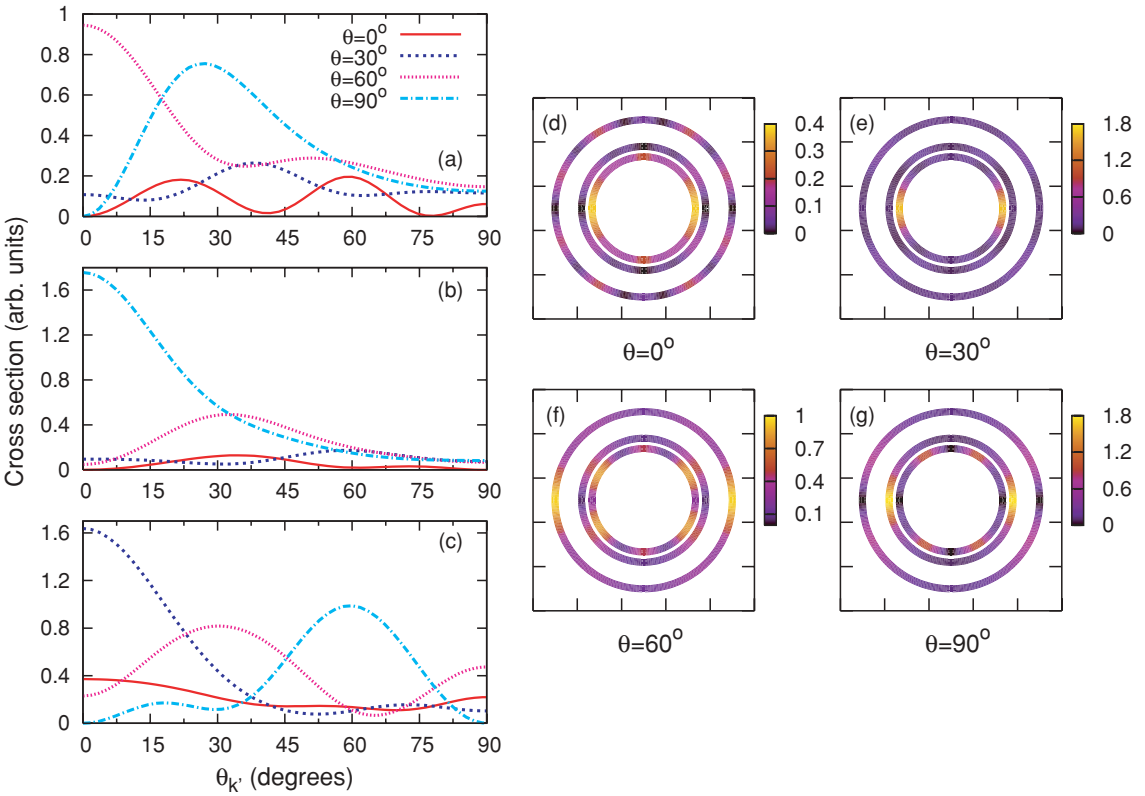

FIG. 8. (Color online) Photoionization cross sections in the laboratory frame for single-photon (43-eV) ionization of fixed-in-space CO_2 vs emission angle $\theta_{k'}$ at alignment angles indicated and for ionization leading to CO_2^+, in panels (a)–(c), in the X, A, and B states, respectively. In panels (d)–(g) the same distributions are shown for the X, A, and B channels at each fixed-in-space molecular alignment angle. See text.

fixed aligned angles of $\theta = 0°$, 30°, 60°, and 90°, respectively, together with the PADs for isotropically distributed molecules. As the photon energy changes, the PADs also vary substantially at each alignment angle. At 30 eV, as shown in Lucchese *et al.* [10], there is a $3\sigma_g \rightarrow k\sigma_u$ resonance in the HOMO channel. From Fig. 7(e), we further demonstrate that this resonance occurs for small alignment angles only. From Fig. 7, it is clear that the PADs for aligned molecules are quite complicated. The PAD changes much with photon energy as well as with alignment angle. Thus in trying to understand the dynamics of a molecule, measurements that do not explore the alignment dependence will tend to miss important features.

F. PADs of transiently aligned CO_2 molecules in the laboratory frame

In Fig. 8, we show the PADs in the laboratory frame for CO_2 ionized by a 43-eV photon. The three ionization channels considered are $X^2\Pi_g$, $A^2\Pi_u$ and $B^2\Sigma_u^+$, with ionization potential of 13.8, 17.7, and 18.2 eV, respectively [11,47]. In Figs. 8(a)–8(c), the PADs are shown at alignment angles $\theta = 0°$, 30°, 60°, and 90°, respectively. In Figs. 8(d)–8(g) the PADs from the three channels are compared together using false colors. The radius of the circle is a measure of the energy of the photoelectron.

In Figs. 9(a)–9(c), we show the calculated PADs for CO_2 molecules aligned by a pump laser at the time delay of $\tau = 20.82$ and 22.14 ps when molecules are aligned and antialigned, as well as when molecules are isotropically distributed. The PADs are compared together in Figs. 9(d) and 9(e), and vs the time delay in Figs. 9(f)–9(h). The asymmetry parameters, $\beta_{k'}$, in Eq. (24), which be deduced from Figs. 9(a)–9(c), are 0.92, 1.32, and 0.68 for X, A, and B states, respectively [11]. Since the angular distribution of molecules can be considered as known, in the future when experimental data similar to Figs. 9(f)–9(h) become available, one may deconvolute the experimental results to retrieve the alignment dependence of the PADs and compare with the calculated values. Note that with higher alignment, we can also expect sharper features in the PADs, as in the N_2 case shown in Fig. 6.

IV. SUMMARY AND OUTLOOK

In this paper we study photoelectron angular distributions (PADs) from aligned molecules. These data can provide much more detail on the molecule than PADs from isotropically distributed molecules [5]. Since field-free molecular alignment can only be achieved by an IR laser, PADs from aligned molecules can be measured only at strong field IR laser facilities. The IR laser can be used to align molecules, to generate soft x-ray or XUV photons, and to ionize aligned molecules. Experiments have been carried out to determine the total ionization yield from such aligned molecules. With higher intensity of XUV photons or soft x-ray becoming available, one can measure the PADs from aligned molecules. In fact,

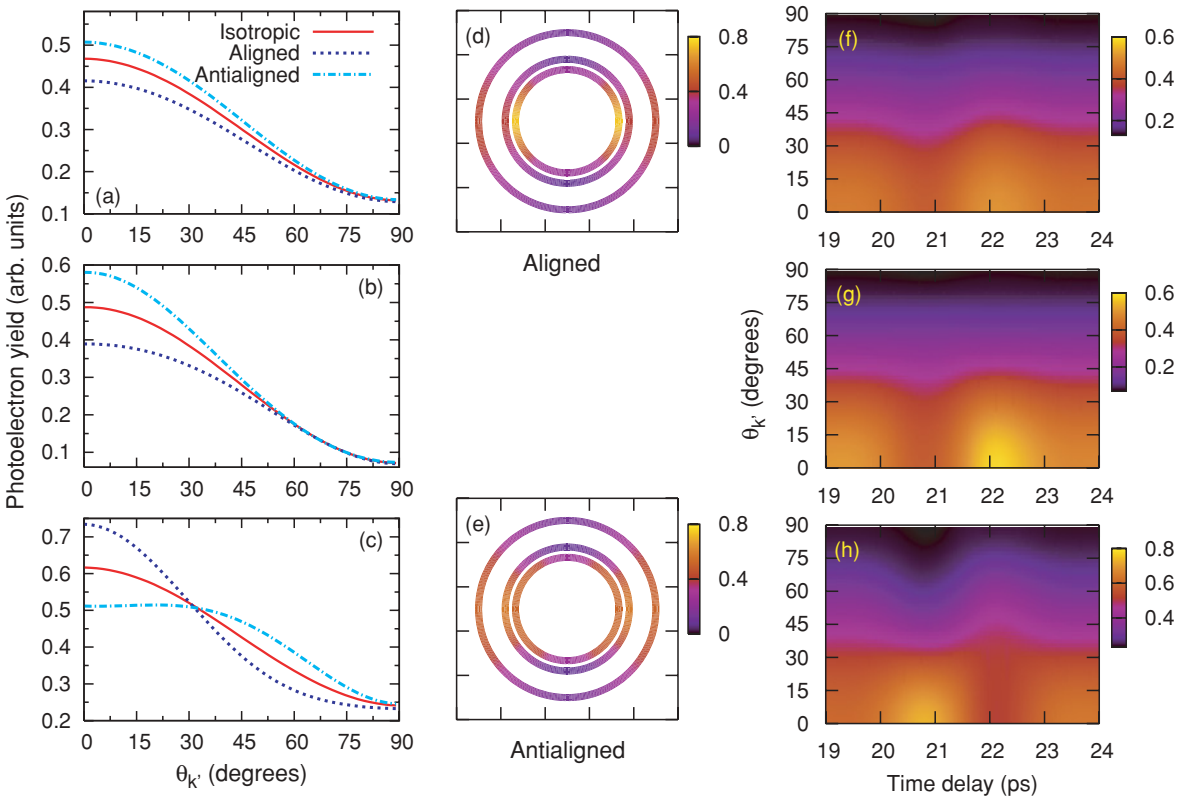

FIG. 9. (Color online) PADs in the laboratory frame for single-photon (43-eV) ionization of CO_2 as a function of emission angle $\theta_{k'}$ and pump-probe time delay. (a)–(c): Molecules are maximally aligned ($\tau = 20.82$ ps), antialigned ($\tau = 22.14$ ps), and isotropically distributed, for ionization leading to CO_2^+ ions in the X, A, and B states, respectively. (d) and (e): The same distributions are compared for maximally aligned and antialigned molecules. (f)–(h): PADs vs time delay for the X, A, and B channels, respectively.

such measurement is already underway [50]. We calculate PADs theoretically for geometries where the PAD can be measured in the future. Using aligned linear molecules such as N_2 and CO_2, we calculate the expected PADs for the removal of one electron from the HOMO, HOMO-1, and HOMO-2 orbitals, by photoionization codes that have been developed. These theoretical predictions often have not been tested except for randomly distributed molecules. In the future, PADs from aligned molecules that are also undergoing changes in the vibrational degrees of freedom can also be measured. In fact, such experiments have been demonstrated by Bisgaard *et al.* [12], and PADs will be able to provide insights into the time-dependent systems. With these possibilities, the well-tested PAD measurements of isotropically distributed molecules are expected to play important roles in structure determination of molecules.

ACKNOWLEDGMENTS

This work was supported in part by the Chemical Sciences, Geosciences and Biosciences Division, Office of Basic Energy Sciences, Office of Science, US Department of Energy. R.R.L. also acknowledges the support of the Robert A. Welch Foundation (Houston) under Grant No. A-1020.

[1] A. Stolow and J. G. Underwood, Adv. Chem. Phys. **139**, 497 (2008).
[2] K. L. Reid, Annu. Rev. Phys. Chem. **54**, 397 (2003).
[3] D. M. Neumark, Annu. Rev. Phys. Chem. **52**, 255 (2001).
[4] M. Tsubouchi and T. Suzuki, Phys. Rev. A **72**, 022512 (2005).
[5] D. Dill, J. Chem. Phys. **65**, 1130 (1976).
[6] F. Rosca-Pruna and M. J. J. Vrakking, J. Chem. Phys. **116**, 6567 (2002).
[7] B. Friedrich and D. Herschbach, Phys. Rev. Lett. **74**, 4623 (1995).
[8] H. Stapelfeldt and T. Seideman, Rev. Mod. Phys. **75**, 543 (2003).
[9] I. Thomann, R. Lock, V. Sharma, E. Gagnon, S. T. Pratt, H. C. Kapteyn, M. M. Murnane, and W. Li, J. Phys. Chem. A **112**, 9382 (2008).
[10] R. R. Lucchese, G. Raseev, and V. McKoy, Phys. Rev. A **25**, 2572 (1982).
[11] R. R. Lucchese and V. McKoy, Phys. Rev. A **26**, 1406 (1982).
[12] C. Z. Bisgaard, O. J. Clarkin, G. Wu, A. M. D. Lee, O. Geßner, C. C. Hayden, and A. Stolow, Science **323**, 1464 (2009).
[13] O. Geßner *et al.*, Science **311**, 219 (2006).

[14] M. Meckel *et al.*, Science **320**, 1478 (2008).
[15] V. Kumarappan, L. Holmegaard, C. Martiny, C. B. Madsen, T. K. Kjeldsen, S. S. Viftrup, L. B. Madsen, and H. Stapelfeldt, Phys. Rev. Lett. **100**, 093006 (2008).
[16] A. T. Le, R. R. Lucchese, and C. D. Lin, J. Phys. B **42**, 211001 (2009).
[17] H.-J. Werner *et al.*, MOLPRO, Version 2002.6, A Package of *Ab Initio* Programs, Birmingham, UK, 2003.
[18] R. E. Stratmann, R. W. Zurales, and R. R. Lucchese, J. Chem. Phys. **104**, 8989 (1996).
[19] B. Basden and R. R. Lucchese, Phys. Rev. A **37**, 89 (1988).
[20] G. Bandarage and R. R. Lucchese, Phys. Rev. A **47**, 1989 (1993).
[21] R. E. Stratmann and R. R. Lucchese, J. Chem. Phys. **102**, 8493 (1995).
[22] A. D. Bandrauk and J. Ruel, Phys. Rev. A **59**, 2153 (1999).
[23] T. Seideman, Phys. Rev. Lett. **83**, 4971 (1999).
[24] H. Stapelfeldt and T. Seideman, Rev. Mod. Phys. **75**, 543 (2003).
[25] J. Ortigoso, M. Rodriguez, M. Gupta, and B. Friedrich, J. Chem. Phys. **110**, 3870 (1999).
[26] J. O. Hirschfelder, C. F. Curtiss, and R. B. Bird, *Molecular Theory of Gases and Liquids* (Wiley, New York, 1954).
[27] *NIST Chemistry WebBook*, NIST Standard Reference Database No. 69, edited by P. J. Linstrom and W. G. Mallard (National Institute of Standards and Technology, Gaithersburg, MD, 2006), p. 20899; http://webbook.nist.gov.
[28] X. M. Tong and S. I. Chu, Chem. Phys. **217**, 119 (1997).
[29] X. M. Tong and Shih-I Chu, Phys. Rev. A **61**, 031401(R) (2000).
[30] S. Wallace and D. Dill, Phys. Rev. B **17**, 1692 (1978).
[31] P. B. Corkum, Phys. Rev. Lett. **71**, 1994 (1993).
[32] J. L. Krause, K. J. Schafer, and K. C. Kulander, Phys. Rev. Lett. **68**, 3535 (1992).
[33] M. Lewenstein, Ph. Balcou, M. Yu. Ivanov, A. L'Huillier, and P. B. Corkum, Phys. Rev. A **49**, 2117 (1994).
[34] T. Morishita, A. T. Le, Z. Chen, and C. D. Lin, Phys. Rev. Lett. **100**, 013903 (2008).
[35] A. T. Le, R. R. Lucchese, S. Tonzani, T. Morishita, and C. D. Lin, Phys. Rev. A **80**, 013401 (2009).
[36] X. M. Tong, Z. X. Zhao, and C. D. Lin, Phys. Rev. A **66**, 033402 (2002).
[37] S. F. Zhao, C. Jin, A. T. Le, T. F. Jiang, and C. D. Lin (unpublished); e-print arXiv:1001.3862.
[38] B. K. McFarland, J. P. Farrell, P. H. Bucksbaum, and M. Gühr, Science **322**, 1232 (2008).
[39] X. Zhou, R. Lock, W. Li, N. Wagner, M. M. Murnane, and H. C. Kapteyn, Phys. Rev. Lett. **100**, 073902 (2008).
[40] X. Zhou, R. Lock, N. Wagner, W. Li, H. C. Kapteyn, and M. M. Murnane, Phys. Rev. Lett. **102**, 073902 (2009).
[41] J. Levesque, D. Zeidler, J. P. Marangos, P. B. Corkum, and D. M. Villeneuve, Phys. Rev. Lett. **98**, 183903 (2007).
[42] J. Itatani, D. Zeidler, J. Levesque, M. Spanner, D. M. Villeneuve, and P. B. Corkum, Phys. Rev. Lett. **94**, 123902 (2005).
[43] T. Kanai, S. Minemoto, and H. Sakai, Nature (London) **435**, 470 (2005).
[44] W. Boutu *et al.*, Nature Phys. **4**, 545 (2008).
[45] O. Smirnova, Y. Mairesse, S. Patchkovskii, N. Dudovich, D. Villeneuve, P. Corkum, and M. Yu. Ivanov, Nature (London) **460**, 972 (2009).
[46] C. Jin, A. T. Le, and C. D. Lin, Phys. Rev. A **79**, 053413 (2009).
[47] D. W. Turner, C. Baker, A. D. Baker, and C. R. Brundle, *Molecular Photoelectron Spectroscopy: A Handbook of He 584 Å Spectra* (Wiley, London, 1970).
[48] A. T. Le, R. R. Lucchese, M. T. Lee, and C. D. Lin, Phys. Rev. Lett. **102**, 203001 (2009).
[49] E. Gagnon, P. Ranitovic, X. M. Tong, C. L. Cocke, M. M. Murnane, H. C. Kapteyn, and A. S. Sandhu, Science **317**, 1374 (2007).
[50] M. Vrakking (private communication).